

## THINNING OF CURRENT SHEETS AND MAGNETIC RECONNECTION

Nagendra Singh,<sup>1,2</sup> and Chakri Deverapalli<sup>2</sup>

Department of Electrical and Computer Engineering<sup>1</sup> and CSPAR<sup>2</sup>,  
University of Alabama, Huntsville, AL 35899, USA.  
e-mail- [singh@ece.uah.edu](mailto:singh@ece.uah.edu)

**Abstract.** Using three-dimensional particle-in-cell (3DPIC) simulations, we study the formation of a thin current sheet. The processes associated with thin current sheets reported here include its thinning, associated potential well in its central part, ion acceleration into the well, current-driven ion mode instabilities, electron and ion heating, current sheet re-broadening, current disruption in the central part of the current sheet and magnetic reconnection. It is shown that current driven instabilities become explosive when the preferential heating of electrons by the ions make electron temperature higher than that of the ions. This explosive stage is associated with high plasma resistivity, current disruption and bifurcated current sheets. The current disruption is linked to the magnetic reconnection.

### Introduction

Previously we have reported the electro-dynamic processes in a thin current sheet (CS) of thickness  $L \sim \lambda_e$ , the electron skin depth. The processes include the enhanced level of anomalous plasma resistivity just before the explosive magnetic reconnection (MR) of anti-parallel magnetic fields accompanied with current disruption and bifurcation of the CS<sup>1</sup>. In this previous study we had artificial ion to electron mass ratio  $M/m=16$ , a major persistent drawback of PIC simulations. In our new simulations reported here we have not only used real mass ratio  $M/m=1836$  for a  $H^+$  plasma, but we have also simulated wider CSs. These improvements have yielded a much clearer picture of the CS evolution nicely separating the various stages of the CS evolution, including its thinning, electron and ion heating inside it, effect of the heating on the evolution of the current-driven instabilities, re-widening of the CS, current disruption in its central region resulting into its bifurcation. The explosive growth in the anomalous resistivity and simultaneous magnetic reconnection occur when the preferential electron heating by the current driven instability begins to yield electron temperatures higher than that for the initially hot ions. These findings from our 3-D simulations yield self-consistent physics of MR.

### Method of Simulation

We utilized a fully 3-D electromagnetic PIC code with relativistic effects included<sup>2</sup>. We simulate a three-dimensional (3-D) volume  $L_x \times L_y \times L_z$  with anti-parallel magnetic field given by

$$B = B_0 \tanh[(z - z_c)/L] a_x, \quad (1)$$

where  $B_0$  is the magnetic field at distances far away from the central plane  $z = z_c = L_z / 2$ ,  $a_x$  is unit vector along the x axis,  $L$  is the scale length in the variation of the x-component of the magnetic field,  $B_x$ , with  $z$ . The field in (1) is always maintained through the entire simulation time as an external source for driving the plasma. In the simulations the grid spacing is the Debye length,  $\lambda_{do}$ , in the initial plasma with a

uniform density  $n_0$  and Maxwellian electrons and ions having temperatures  $T_e$  and  $T_i$ , respectively;  $T_i/T_e = 2$ . We incorporated periodic boundary conditions along x and y on both particles and fields. Along z we used a conducting boundary conditions for the fields while the particle boundary conditions were varied in different simulations. In the simulations described here the particles leaving the simulation box at boundaries  $z = 0$  and  $L_z$  are not re-circulated, instead they are replaced by new ones from the Maxwellian distributions having the same temperatures as the initial plasma loaded in the simulation box. The fields in this code are updated solving the time-dependent Maxwell's equations, including a correction for the space-charge field<sup>3</sup>.

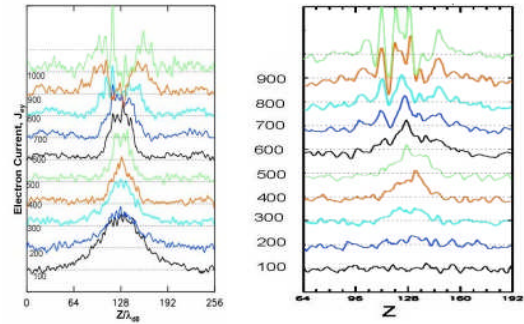


Fig. 1. (a) Evolution of current distribution in the CS,  $J_y(z)$ . Note the thinning of the CS till  $t \sim 500 \omega_{pe}^{-1}$  is followed by re-broadening until  $t \sim 800 \omega_{pe}^{-1}$  and subsequent bifurcation when the current disrupts in the central CS. (b) Evolution of plasma density. Note that the density is enhanced in the central part of the CS after  $t \sim 200 \omega_{pe}^{-1}$ . The times labeled on the panels are in the units of  $\omega_{pe}^{-1}$  and the distances in Debye length  $\lambda_{do}$ .

For future reference we point out the following spatial and temporal scales in the simulation: electron skin depth  $\lambda_e = 10 \lambda_{do}$ , ion skin depth  $\lambda_i = 428 \lambda_{do}$ , electron Larmor radius  $\rho_e \geq 2 \lambda_{do}$ , ion Larmor radius  $\rho_i \geq 120 \lambda_{do}$ , electron plasma period  $\tau_{pe} = 6.28 \omega_{pe}^{-1}$ , electron cyclotron period  $\tau_{ce} = 12.5 \omega_{pe}^{-1}$ , ion plasma period  $\tau_{pi} = 270 \omega_{pe}^{-1}$ , and ion cyclotron period  $\tau_{ci} = 22950 \omega_{pe}^{-1}$ . Simulation is advanced in time with a time step  $\Delta t = 0.02 \omega_{pe}^{-1}$ . Here  $\omega_{pe}$  is the electron plasma frequency,  $V_{teo}$

is the electron thermal velocity and  $\lambda_{do} = V_{teo}/\omega_{po}$ , all in the initial plasma.

### Current sheet thinning and potential well formation

We describe here results from a simulation with the thickest CS simulated so far, namely,  $L = 3.6\lambda_e$ . Thin CSs with such a thickness have been observed from Cluster<sup>4,5</sup>. Fig. 1a shows the evolution of the current profile  $J_y(z)$  averaged over the x-y plane. Over the time period shown in Fig. 1a, electrons primarily carry  $J_y$  and not the ions. The evolution of the plasma density associated with  $J_y(z)$  is shown in Fig. 1b. Using Ampere's law ( $\nabla \times B = \mu_0 J$ ) the maximum current density expected for the magnetic field  $B_x(z)$  in (1) is  $J_{y\max} = B_0/\mu_0 L$ , which for  $L = 36\lambda_{do} = 3.6\lambda_e$  gives  $J_{y0} = [0.5(C/V_{teo})^2/L] J_{th} = 1.38 J_{th}$ , where  $J_{th} = n_0 e V_{teo}$ . Fig. 1a shows that for  $t \geq 100\omega_{po}^{-1}$  the maximum current density settles down to  $J_{y\max} \sim 2 J_{th}$  and it remains so until  $t = 500\omega_{po}^{-1}$ ; this current being larger than  $J_{y0}$  implies thinning of the CS. The width of Fig. 2. The top panel shows magnetic field profiles from (1) in blue (dot-dashed) and at  $t = 500\omega_{po}^{-1}$  (solid) along with its Harris fit (dashed). The bottom panel shows the currents corresponding to the B profiles.

the current pulse continues to thin until  $t = 500\omega_{po}^{-1}$ . The current distribution tends to re-broaden with the maximum current remaining the same until  $t \sim 700\omega_{po}^{-1}$  and then sharply reducing after  $t \sim 800\omega_{po}^{-1}$ . The current in the central part of the CS eventually completely disrupts leaving a bifurcated CS.

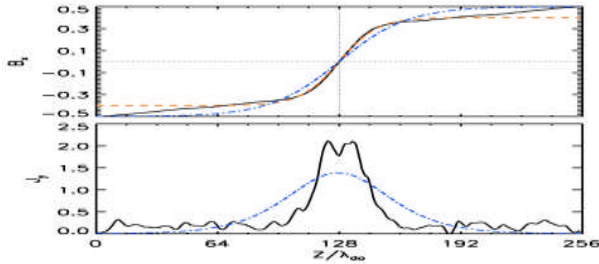


Fig. 2. The top panel shows magnetic field profiles from (1) in blue (dot-dashed) and at  $t = 500\omega_{po}^{-1}$  (solid) along with its Harris fit (dashed). The bottom panel shows the currents corresponding to the B profiles.

Fig. 2 shows the profiles given by (1) (blue) and that (solid line) associated with the current distribution at  $t = 500\omega_{po}^{-1}$  when it is the thinnest (Fig. 1a). The current distributions  $J_y(z)$  corresponding to these magnetic field distributions are plotted in b; the maximum current at  $t = 500\omega_{po}^{-1}$  is  $J_y \sim 2.1 J_{th}$  while for the magnetic field in (1) it is  $1.38 J_{th}$ , indicating that the magnetic field profile at  $t = 500\omega_{po}^{-1}$  is steepened. The profile for the magnetic field at  $t = 500\omega_{po}^{-1}$  is also fitted with Harris ( $\tanh(\cdot)$ ) profile (red dashed line) showing that the half width is reduced from  $36\lambda_{do} = 3.6\lambda_e$  to  $\sim 23\lambda_{do} \approx 2\lambda_e$ .

The thinning is caused by plasma flows from the outer regions of the CS to its central region near  $z \sim L_z/2 = 128\lambda_{do}$ . The flow develops due to the  $\mathbf{J} \times \mathbf{B}$  force on the current-carrying magnetized electrons. This force brings electrons into the central region, making it electrically negative with respect to the outer regions. Thus the unmagnetized ions flow into this region creating a counter-streaming ion population in

the central region. Ions eventually get trapped in the growing negative potential well in the central region. This process accumulates plasma in the central region of the CS enhancing the density there (Fig. 1b); the maximum density in the center becomes  $\sim 2n_0$  as seen from the density profiles in Fig. 1b. Fig. 3a shows an example of the profile of the potential well,  $\phi(z)$ . The ion acceleration into the negative well is shown by the ions'  $z$ - $V_z$  phase-space plotted in Fig. 3b. The maximum acceleration is seen up to  $|V_z| \sim 0.15V_{teo}$ , which amounts to an ion energy  $W \sim 20 k_B T_0$ , which could be in a few keV range depending on the background electron temperature  $T_0$ . We point out that the potential well evolves with time. The ion-acoustic and Alfvén speeds are  $C_s = 0.06V_{teo}$  and  $V_A = 0.12V_{teo}$ . It appears that current sheet evolves at a time scale determined by the propagation of fast Alfvén mode in the  $z$  direction with a velocity  $V_F = (V_A^2 + C_s^2)^{1/2}$ .

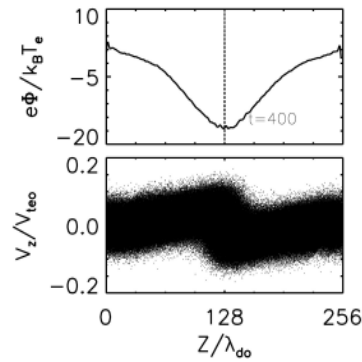


Fig. 3.

(a) Electrostatic potential well associated with the thin CS at  $t = 400\omega_{po}^{-1}$  when it is about the thinnest in the simulation. (b) Acceleration of ions into the potential well is shown by the  $z$ - $V_z$  phase space. Note the counter-streaming of ions accelerated by the inward pointing electric fields  $E_z$ .

The re-broadening for  $t \geq 600\omega_{po}^{-1}$  (Fig. 1a) is caused by the enhanced kinetic pressure due to the heating of electrons and ions in combination with the enhanced density in the central CS. The heating itself is caused by current-driven instabilities. The eventual current disruption in the central region near  $z \sim 128\lambda_{do}$  for  $t \geq 850\omega_{po}^{-1}$  (Fig. 1a) is a consequence of the trapping of electrons in the explosively phase of the current-driven instabilities, which are discussed next.

### Plasma Instabilities

We now examine the temporal and spatial behavior of the plasma instability, which drastically affects the CS and also leads to fast reconnection. Figs. 4a-4c show the temporal evolution of electric fields  $E_x$ ,  $E_y$  and  $E_z$ . The corresponding magnetic field evolution is shown in Figs. 4d-4f. First of all we notice that the fluctuations in the magnetic field components  $b_y$  and  $b_z$  are minimal until  $t \sim 800\omega_{po}^{-1}$  and over the same time period the perturbations in the x-component of the magnetic field,  $b_x$ , are associated with the thinning of the CS (Fig. 1a); this perturbation plus the  $B_x$  given in (1) give the thinned current sheet as seen near  $t \sim 500\omega_{po}^{-1}$  in Figs. 1a and 2. In contrast to this temporal behavior of the magnetic field, the fluctuations in the electric field components in Figs. 4a-4c begin to grow as early as  $t \sim 300\omega_{po}^{-1}$  and they are confined within the central region of the CS. Thus the instability starts out as purely electrostatic (ES).

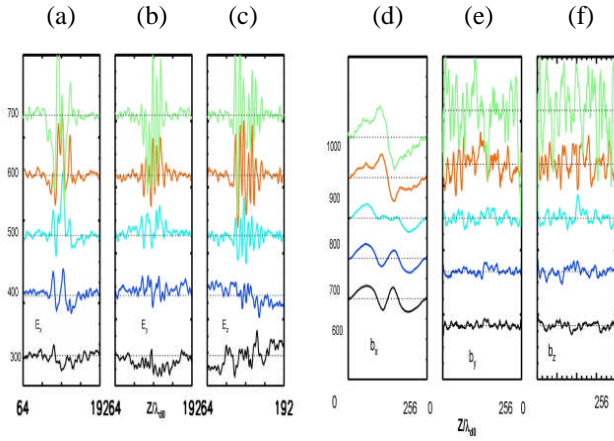


**Fig. 4.** Temporal evolution of fluctuations in electric fields (a)  $E_x$ , (b)  $E_y$ , (c)  $E_z$  and magnetic fields (d)  $b_x$ , (e)  $b_y$  and (f)  $b_z$ .

The electric field perturbations are found to be nearly purely growing modes. We have interpreted the growth in the fluctuations in the electric field as ion modes driven by the current in plasmas<sup>1,6</sup>. Such ion modes are related to Buneman instability<sup>7</sup>, which has well-known growth rate and dispersion behavior derived from cold plasma dispersion relation. However, in our simulations cold-plasma conditions are not met. Fig. 5a shows an example of the electron and ion velocity distribution functions at  $t=500\omega_{pe}^{-1}$ ; the electron and ion average drifts and temperatures are also indicated in the Fig. 5a; drift  $V_{edy}=-1.045V_{teo}$ , electron temperature  $T_{ey}=2.34T_0$  and ion temperature  $T_{iy}=2T_0$ . Note that the electrons are already heated and but not the ions as they still have the initial  $T_{iy}$ . The temporal evolution of the drift  $V_{edy}$  and electron and ion temperatures  $T_{ey}$  and  $T_{iy}$  are shown in Figs. 5b and 5c. Note that initially we have  $T_{ey}/T_{iy}=0.5$  and  $T_{ey}$  remains smaller than  $T_{iy}$  until  $t\sim 500\omega_{pe}^{-1}$ . Eventually for  $t\geq 500$  the heated electrons have  $T_{ey}/T_{iy}\geq 1$ , which reduces the threshold for the instability. Since  $J_y$  (Fig. 1a) and the drift  $V_{edy}$  remain nearly constant over  $300\omega_{pe}^{-1} < t < 700\omega_{pe}^{-1}$  (Fig. 5c), the increasing  $T_{ey}/T_{iy}$  (Fig. 5b) escalates the growth of the waves (Figs. 4a-4c) after  $t\sim 500\omega_{pe}^{-1}$ .

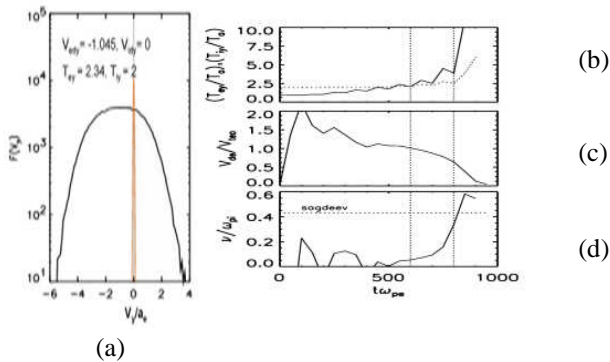


**Fig. 5.** (a) Electron and ion Velocity distribution functions. Temporal evolution of (b) electron (solid) and ion (dotted) temperatures  $T_{ey}$  and  $T_{iy}$ , (c) relative drift  $V_{de}$  between electrons and ions and (d) anomalous collision frequency  $\nu_a$ .

Since the current distribution  $J_y(z)$  is non-uniform and electron drift has shear, it is not possible to directly apply the

results of linear instability in an uniform plasma<sup>6,7</sup>. Our simulations reveal the nature of the instability including the complexity of the CS structure. We find that the growth of the instability escalates as the electrons, initially colder than the ions, are heated by the instability and especially when  $T_{ey}$  overtakes the ion temperature  $T_{iy}$  (Fig. 5b). The spatial structure of the instability is shown in Fig. 6a-6c, in which  $E_x$ ,  $E_y$ , and  $E_z$  are plotted in the  $x$ - $z$  ( $y=16$ ) (top) and  $x$ - $y$  ( $z=128$ ) (bottom) planes, respectively. The growing oscillations are confined in the central region of the CS as shown by the top panels in Fig. 6.

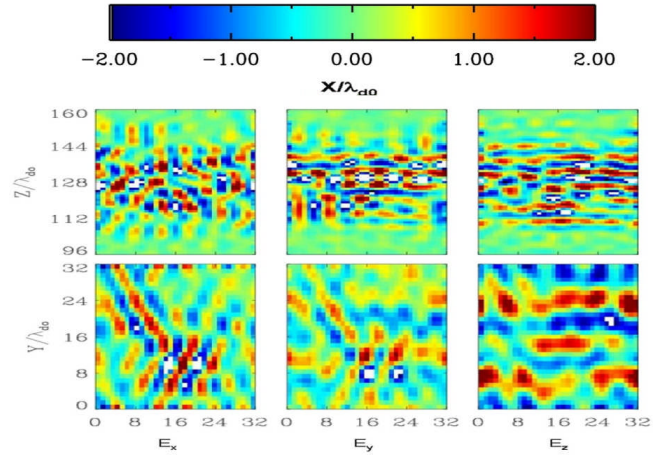


**Fig. 6.** Spatial structure of the growing oscillations at  $t=700$ : top panels from left to right show  $E_x(x,z)$ ,  $E_y(x,z)$  and  $E_z(x,z)$ , all at  $y=16$  in the  $x$ - $z$  plane. Bottom panels show the same fields in the  $x$ - $y$  plane at  $z=128$ . The color bar at the top shows the normalized amplitudes.

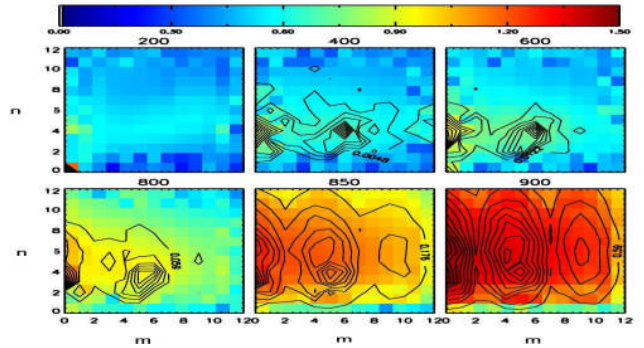


**Fig. 7.** The growth in the amplitude of  $E_y(x,y)$  is shown by the Fourier spectrum in the  $m$ - $n$  plane where  $m$  and  $n$  give the mode numbers along  $x$  and  $y$ , respectively.

The growth of the instability in the wave number plane  $k_x$ - $k_y$  is shown in Fig. 7, in which 2-D Fourier transform of the data like that in the bottom panel of Fig. 6b is plotted at some selected times. Note that  $k_x = m \times 2\pi/L_x$  and  $k_y = n \times 2\pi/L_y$ , where  $m$  and  $n$  are the mode numbers. Initially the dominant modes occur over  $2 < n < 4$ , giving  $0.4 < k_y \lambda_{d0} < 0.8$ . Along  $x$  the mode structure allows for  $k_x \lambda_{d0} \sim 1$  or  $m=5$ . Such wave numbers are comparable with the wave numbers expected for the Buneman and ion acoustic instabilities<sup>6,7</sup> giving  $k_y \sim \omega_{pe}/V_{dey}$ . Fig. 7 shows a sudden characteristic change in the wave structure at  $t\sim 800$ ; this is the time when the electron temperature  $T_{ey}$  significantly exceeds  $T_{iy}$  and the instability escalates and



reconnection occurs in the CS. Fig. 8 shows the vector plots of the magnetic field in the x-z plane. Prior to  $t=700$ , B vectors are aligned with the x-axis all over the x-z plane. At  $t=800$  we see the formation of x line, which is stretched over  $8 < x < 24$ .

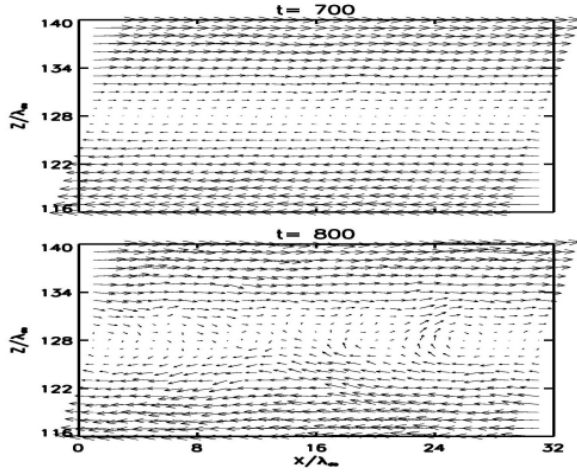


**Fig. 8.** Vector plot of  $\mathbf{B}$  in the x-z plane at  $t=700\omega_{po}^{-1}$  (top) and  $t=800\omega_{po}^{-1}$  (bottom). Prior to  $t \sim 700\omega_{po}^{-1}$ ,  $\mathbf{B}$  remains aligned along x. Rather suddenly the vectors rotate over  $8 < x < 24$  in the central CS and reconnection occurs.

### Anomalous Resistivity

We now discuss the generation of anomalous resistivity in the CS. Fig. 5b shows the plots of electron drift as a function of time. We measure the anomalous resistivity by calculating the rate of change in the average electron momentum lying over  $112 < z < 144$  in the center of the CS. This gives us the anomalous collision frequency  $\nu_a = -V_{de}^{-1} dV_{de}/dt$ . Fig. 5c shows the temporal evolution of the anomalous collision frequency  $\nu_a(t)$ . We find that  $\nu_a$  fluctuates before  $t \sim 500\omega_{po}^{-1}$ , but after this time  $\nu_a$  grows faster and faster until  $t \sim 850\omega_{po}^{-1}$ , when the reconnection has already set in the simulation. The maximum anomalous frequency reaches a value as high as  $\nu_{max} \sim 0.6\omega_{pi}$ , where  $\omega_{pi}$  is the ion plasma frequency. For the purpose of comparison, we have plotted the analytical value of  $\nu_a$  based on nonlinear evolution of the ion-acoustic instability<sup>8</sup>; similar values of  $\nu_a$  have been reported from 1-D Vlasov simulations<sup>9</sup>. We emphasize that  $\nu_a$  evolves with the changing electron and ion temperatures in the CS; it is not a static quantity.

### Conclusion and Discussion

Using 3D kinetic simulations we have studied the basic plasma processes involved in the formation of a thin current sheet, development of current-driven instabilities in it, electron and ion heating in side the sheet, development of anomalous resistivity during an explosive phase of the current-driven instability and finally magnetic reconnection. We drive the simulation by an imposed antiparallel magnetic field. One would normally expect that the scale length of this applied field should determine the scale length of the current

sheet. However, we find that the current sheet underwent considerable thinning.

Another important process revealed by our simulations is the formation of a potential well in the central part of the CS. We reported this in a previous paper<sup>1</sup>. However, in this previous work the simulations were performed for an artificially low ion to electron ratio of  $M/m=16$ ; therefore, the many of the processes reported were compressed in time. The potential well is a direct consequence of the electron transport in to the central region by the  $\mathbf{J} \times \mathbf{B}$  force on the magnetized electrons. The potential well accelerates the unmagnetized ions into the central part of the CS and traps them there. Wygant et al.<sup>4</sup> have emphasized this feature of very thin current sheets in the magneto-tail.

The re-broadening of the CS, current disruption in its central part and its bifurcation are yet another set of processes, which are a direct consequence of the formation of the thin CS. A very thin CS with large current density has sufficiently large relative drift between electrons and ions. Our simulations show that such drifts in a CS are able to drive Buneman and ion-acoustic type ion modes<sup>6</sup> despite the fact that initially ions are hotter than the electrons. When the instability begins they first preferentially heat the electrons and electron temperature  $T_{ey}$  becomes progressively higher than that of the ions ( $T_{iy}$ ), then the growth rate of the instability becomes explosive. Previously Singh<sup>1</sup> attributed the growth rate to the developing shear in the electron drift. It is quite possible that both evolving shear and the ratio  $T_{ey}/T_{iy}$  combine to make the instability explosive. In this stage of the instability the plasma in the central CS become highly resistive. The instability causes current disruption by trapping electrons. The current disruptions are found to be the major cause of the collisionless magnetic reconnection in our simulations. The current disruption is also the primary cause of the bifurcation of the very thin current sheet. Starting from the ISEE observations<sup>10</sup>, now there are several reports on bifurcated current sheets from Geotail<sup>11</sup> and Cluster<sup>4,12</sup>. The observation of bifurcated current sheets reported by Wygant et al.<sup>4</sup> directly deal with very thin current sheets like seen in our simulations.

### References

1. Singh, N., *Nonl. Proc. Geophys.*, **11**, 153-163, (2004).
2. Birdsall, C. K. and Langdon, A. B.: *Plasma Physics via Computer Simulations*, NY, McGraw-Hill, 1985.
3. Langdon, A. B., *Compt. Phys. Commun.*, **70**, 447(1992).
4. Wygant T. J., et al., *J. Geophys. Res.*, **110**, A09206, doi:10.1029/2004JA010708 (2005).
5. Nakamura, R., et al. <http://www.glue.umd.edu/~sitnov/TCS/tcs.1.files/online.htm>, (2004).
6. Fried, B. D., and R. W. Gould, *Phys. Fluids*, **4**, 139(1961)
7. Buneman, O., *Phys. rev.*, **115**, 503 (1959).
8. Papadopoulos, K., *Rev. Geophys. Space Phys.*, **15**, 113(1977).
9. Watt, C.E.J., R.B. Horne, and M.P. Freeman, *Geophys. Res. Lett.*, **29**, 10.1029, 2002.
10. Hosino, M., et al., *J. Geophys. Res.*, **101**, 24775 (1996).
11. Asano, Y., et al., *J. Geophys. Res.*, **108**, doi:10.1019/2002JA009785, 2003.
12. Runov, A. et al., *Geophys. Res. Lett.*, **30**, 1036, doi: 10.1029/2002GL016136, (2003).